CrystEngComm

Accepted Manuscript

ROYAL SOCIETY OF CHEMISTRY

www.rsc.org/crystengcomm

Graphic abstract

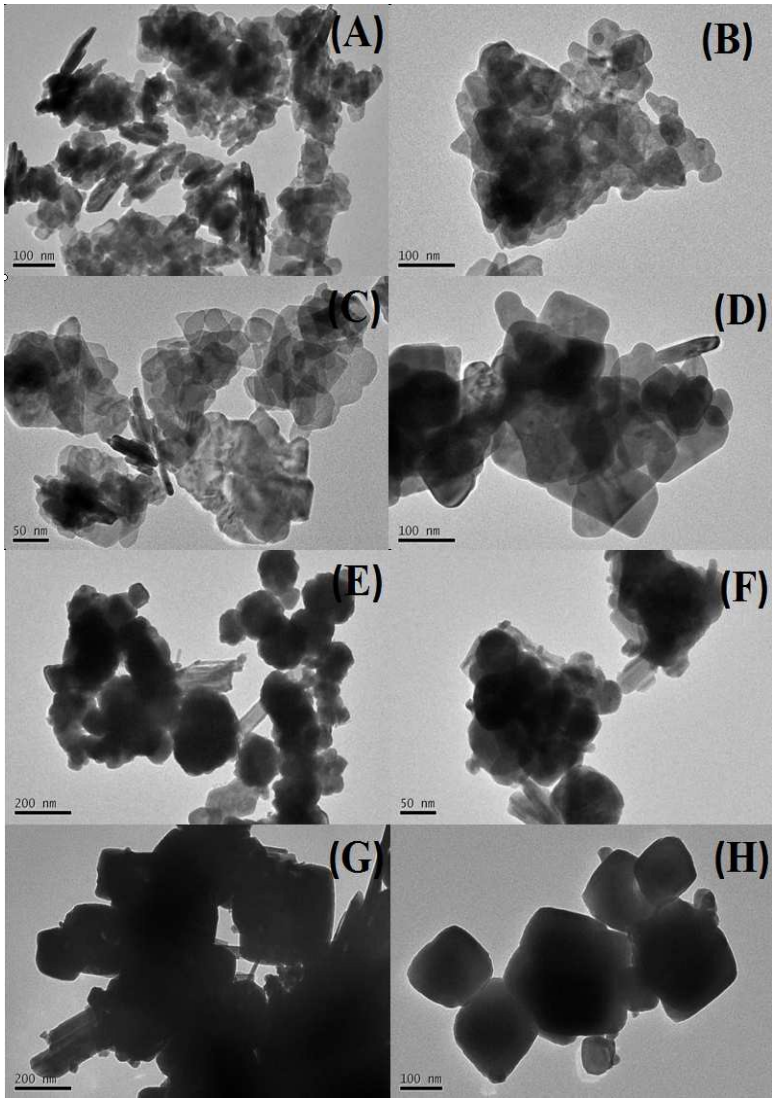

Influence of Phase Structure and Morphology on photocatalytic Activity of Bismuth Molybdates

Daimei Chen[1], Qiang Hao, Zhihong Wang[1,2], Hao Ding[1], Yongfa Zhu[2]**

([1]National Laboratory of Mineral Materials, School of Materials Sciences and Technology, China University of Geosciences, Beijing 100083, China

[2]Department of Chemistry, Tsinghua University, Beijing, 100084, PR China)

*Corresponding author.

Tel.: +86 10 82332274; fax: +86 10 82322974.

[1] E-mail: chendaimei@cugb.edu.cn;
[2] E-mail: zhuyf@tsinghua.edu.cn

Abstract:

The bismuth molybdates photocatalysts with the different phase structures and morphologies were controllably synthesized via the refluxing method by adjusting the pH in the reaction system. The Bi_2MoO_6 nanosheets were easily obtained under acidic condition, while $Bi_{3.64}Mo_{0.36}O_{6.55}$ nanoparticles were formed under circumneutral and basic solution. The mechanism for the formation and phase transition of these two bismuth molybdates is that tuning the pH value can control the growth rates along different crystal axes and the different hydrolysis products as the initial seed of crystallographic phase. The photocatlytic activity of Bi_2MoO_6 nanosheets for MB and MO degradaiotn was higher than that of $Bi_{3.64}Mo_{0.36}O_{6.55}$ nanoparticles under visible light irradiation, and the highest photocatalytic activity was observed for the Bi_2MoO_6 nanosheet prepared at pH 6.0. The high visible-light photocatalytic activity for Bi_2MoO_6 nanosheet arises from the easy separation and transfer of the photogenerated electron–holes in the nanosheets structure and the narrow band gap leading to the improvement of the visible absorption ability. The electron spin resonance (ESR) and the photogenerated carriers trapping experiment suggested that both Bi_2MoO_6 and $Bi_{3.64}Mo_{0.36}O_{6.55}$ have the same photocatalytic mechanism and the main oxidative species for these samples are hydroxyl radical.

Keyword:

Photocatalyst; Visible-light; Bismuth molybdates; pH value; Morphology

1. Introduction

In recent decades, TiO_2 has been used and investigated widely for the photodegradation of organic pollutants in water owing to its low cost, strong oxidizing power, and nontoxic nature.[1, 2] However, the deficiency of requiring UV light for effective photocatalysis severely hinders the overall process to be used in practical. Therefore, many attempts have been made to prepare visible-light-driven photocatalysts such as $BiVO_4$, $Bi_2Ti_2O_7$, $ZnFe_2O_4$, Bi_2WO_6, bismuth molybdates.[3-7] Among these visible-light catalysts, bismuth molybdates, with the general chemical formula of $Bi_2O_3 \cdot nMoO_3$ (n =1,2,3), have been reported as an excellent photocatalyst and solar-energy-conversion material for water splitting and degradation of organic compounds.[8-10]

Up to now, several bismuth molybdate photocatalysts, including α-$Bi_2Mo_3O_{12}$, β-$Bi_2Mo_2O_9$, γ-Bi_2MoO_6 and $Bi_{3.64}Mo_{0.36}O_{6.55}$ have has been synthesized and studied. Of these bismuth molybdates, only γ-Bi_2MoO_6 has been commonly reported and structurally characterized due to its unique layered structures, narrow band gap and visible-light-response property. Some bismuth molybdates, such as cubic $Bi_{3.64}Mo_{0.36}O_{6.55}$, have seldom been reported. The construction of heterostructured photocatalyst by the combination of cubic phase $Bi_{3.64}Mo_{0.36}O_{6.55}$ and orthorhombic phase Bi_2MoO_6 has shown the greatly improved the visible-light photocatalytic activity.[11,12] In generally, heterostructured photocatalysts containing the same elements but different phases such as $Bi_{3.64}Mo_{0.36}O_{6.55}/Bi_2MoO_6$, $Bi_7O_9I_3/Bi_5O_7I$ and

$BiOBr/Bi_{24}O_{31}Br_{10}$ et al were fabricated by adjusting the phase transformation through controlling the synthesis condition. However, the mechanism of phase transition between these photocatalysts containing the same elements but different phases has seldom been discussed. Furthermore, until now, only a few investigations concerned the preparation and characterization of $Bi_{3.64}Mo_{0.36}O_{6.55}$ as a photocatalyst.[13,14] Therefore, the preparation method and the formation mechanism of $Bi_{3.64}Mo_{0.36}O_{6.55}$ should further be studied. The relationship between the morphology, structure, composite and the photocatalytic activity remain to be clarified.

It is well-known that the photocatalytic property strongly depends on morphology and structure of the catalyst. Therefore, physical and chemical methods such as solvothermal (hydrothermal) reaction,[15-17] solid-state reaction,[18] co-precipitation,[19] sol–gel methods [20] have been used to synthesize the nanostructure Bi_2MoO_6 with the different morphologies. For example, Long et al. [15] synthesized the single crystal Bi_2MoO_6 nanobelts (BMNBs) with dominant (010) facets via oleyamine-mediated hydrothermal method. The experimental result demonstrated that as-prepared BMNBs exhibits higher activity than the counterpart with hierarchical nanorod-based microspheres. Fu and coworkers[7] fabricated the novel hierarchical flower-like Bi_2MoO_6 hollow spheres via a solvothermal process in the presence of ethylene glycol, and showed that the hierarchical flower-like Bi_2MoO_6 hollow spheres exhibited excellent visible-light-driven photocatalytic efficiency for the degradation of Rhodamine B, which was much higher than that of Bi_2MoO_6 prepared by solid-state reaction and TiO_2 (P25). Zhu et al [16] transformed the Bi_2MoO_6 morphology from a 2D

sheet-like structure to a 1D rod-like through a facile, pH-controlled, surfactant-free hydrothermal route. The Bi_2MoO_6 nanosheet prepared under acidic condition exhibited a visible-light photocatalytic activity 12 times higher than Bi_2MoO_6 microrod prepared under basic condition. However, the conventional routes for preparing these catalysts were generally carried out under high temperature and high pressure, which limit the industrial production of the photocatalysts. Therefore, a simple method would need to be developed for the preparation of bismuth molybdates.

In this paper, the refluxing method was developed to controllably synthesize the two different forms of bismuth molybdates (Bi_2MoO_6 and $Bi_{3.64}Mo_{0.36}O_{6.55}$). This method was carried out under the ambient pressure. Thus it is favorable for large-scale industrial production. The morphologies of these bismuth molybdates were tailored by adjusting the pH value of the reaction system. The effect of pH value on the morphology and structure was studied. Furthermore, the relationship among the morphologies, structures and the visible light photoactivities of bismuth molybdates was discussed. The formation mechanism of these two bismuth molybdates was preliminarily explained, and the phase transition mechanism between them was displayed. The visible-light photodegradation mechanism for Bi_2MoO_6 and $Bi_{3.64}Mo_{0.36}O_{6.55}$ was investigated.

2. Experiment section

2.1 Materials Preparation

All the chemicals were of analytic grade without further purification. The

photocatalyst was prepared as follows: an appropriate amount of $Bi(NO_3)_3 \cdot 5H_2O$ and $Na_2MoO_4 \cdot 2H_2O$ were added into 120 mL of the deionized water and were stirred for 10 min at room temperature. The pH of the suspensions was adjusted from 1.00 to 11.00 by adding appropriate amount of HNO_3 and NaOH solution. After being vigorously stirred for 30 min, the resulting precursor suspension was transferred into a 250 mL of three-neck flask, which was subsequently heated at 100 ^oC and refluxed for 12 h. The resultant solid was separated by centrifugation and washed with water, then dried in air at 90 ^oC for 8 h.

2.2 Characterization

X-ray diffraction (XRD) was performed on a Bruker D8-advance diffractometer using Cu Kα radiation (λ=1.5418 Å). Morphologies and structures of the prepared samples were further examined with a JEM-2010 field emission transmission electron microscopy (TEM) operated at an accelerating voltage of 200 kV and SU8010 field emission scanning electron microscope (SEM).The UV–vis diffusion reflection spectra (DRS) of the samples were obtained in the range from 200 to 800 nm by using a Hitachi U-3010 UV-vis spectrophotometer, which is equipped with an integrated sphere attachment and used $BaSO_4$ as the reference sample. The electron spin resonance (ESR) signals of radicals spin-trapped by spin-trap reagent 5,5'-dimethyl-1-pirroline-N-oxide (DMPO) (Sigma Chemical Co.) were examined on a Bruker model ESR JES-FA200 spectrometer equipped with a quanta-Ray Nd: YAG laser system as the irradiation source (λ=420 nm). The same type of quartz capillary tube was used for all ESR measurements to minimize experimental errors. The ESR

spectrometer was coupled to a computer for data acquisition and instrument control. Magnetic parameters of the radicals detected were obtained from direct measurements of magnetic field and microwave frequency. Raman spectra were recorded using a HORIBA JY HR800 confocal microscope Raman spectrometer employing an Ar-ion laser (514.5 nm). All spectra were calibrated with respect to silicon wafer at 520.7 cm^{-1}. Electrochemical impedance spectra (EIS) were measured at 0.0V. A sinusoidal ac perturbation of 5 mV was applied to the electrode over the frequency range of 0.05–10^5 Hz. The Fourier transform infrared (FT-IR) spectra of the samples were recorded on a FT-IR spectrometer using conventional KBr pellets in the wavenumber range of 2000-450 cm^{-1} with a resolution of 1 cm^{-1}. Total organic carbon analyzer (MultiN/C 2100, Jena) was employed for mineralization degree analysis of dye solutions.

2.3 Photocatalytic Tests

The photocatalytic activities were evaluated by the decomposition of methylene blue (MB) and Methyl orange (MO) under visible light irradiation ($\lambda > 420$ nm), respectively. The radial flux was measured by a power meter from the Institute of Electric Light Sources, Beijing. The visible irradiation was obtained from a 500 W xenon lamp (Xujiang Electromechanical Plant, Nanjing, China) with a 420 nm cutoff filter. A 25 mg of photocatalyst was dispersed in an aqueous solution of MB (50 mL, 0.01 mM) totally. Before irradiation, the suspensions were magnetically stirred in the dark for 90 min to reach absorption–desorption equilibrium between the photocatalyst and MB. At certain time intervals, 3 mL aliquots were sampled and centrifuged to

remove the particles. The concentration of the MB was measured by recording the absorbance at the characteristic band of 663 nm by using a Hitachi U-3010 UV−vis spectrophotometer.

The main oxidative species responsible for the photocatalytic activity could be detected by the trapping experiments of active species. Specifically, the hydroxyl radicals (•OH), holes (h^+) and superoxide radical ($O_2•^-$) were investigated by adding 1.0 mM tert-butanol, 1 mM ammonium oxalate ($(NH_4)_2C_2O_4·H_2O$) and purging with N_2 into the MB or MO solution prior to addition of the photocatalyst, respectively.[21,22] The experiment process was similar to the photodegradation experiment.

3. Results and Discussion

3.1 Morphology and structure control

The crystalline structures of the as-prepared samples were examined by X-ray diffraction. Fig. 1 shows XRD patterns of bismuth molybdate samples obtained by refluxing procedure at the different pH. The materials obtained under acidic condition (pH 1.0, pH 3.0, pH 5.0 and pH 6.0) are similar in crystal structure and can be identified as layered orthorhombic Bi_2MoO_6 phase (JCPDS 76-2388).[16] For these samples, the intensity ratio of (1 3 1)/(2 0 0) peaks is below 3.5, while intensity of the (1 3 1) peak of the XRD pattern is about six times stronger than that of the (2 0 0) peak in the standard XRD patterns, implying the special anisotropy of the crystal that grows along the (010) plane.[16] This fact is the direct reason for the formation of sheet-shaped structure of the Bi_2MoO_6 crystallity, which can be confirmed by SEM

and TEM images. Furthermore, the peak intensity increases with pH from 1 to 6, suggesting that the high pH is favorable to the crystal growth. The high crystallity might be favorable to the high photocatalytic activity. When pH increases to 6.5, the characteristic peaks of the Bi_2MoO_6 phase disappear and there appear the mixed phases of $Bi_{3.64}Mo_{0.36}O_{6.55}$ and Bi_2O_3. Further increasing pH from 7.0 to 11.0, the phases of Bi_2MoO_6 and Bi_2O_3 disappear and a new phase attributed to the cubic $Bi_{3.64}Mo_{0.36}O_{6.55}$ (JCPDS 43-0446) occurs.[11] The peaks intensities for the $Bi_{3.64}Mo_{0.36}O_{6.55}$ crystal gradually increase with increasing pH from 7.0 to 11.0, suggesting that alkaline condition is favorable to the formation of $Bi_{3.64}Mo_{0.36}O_{6.55}$ phase.

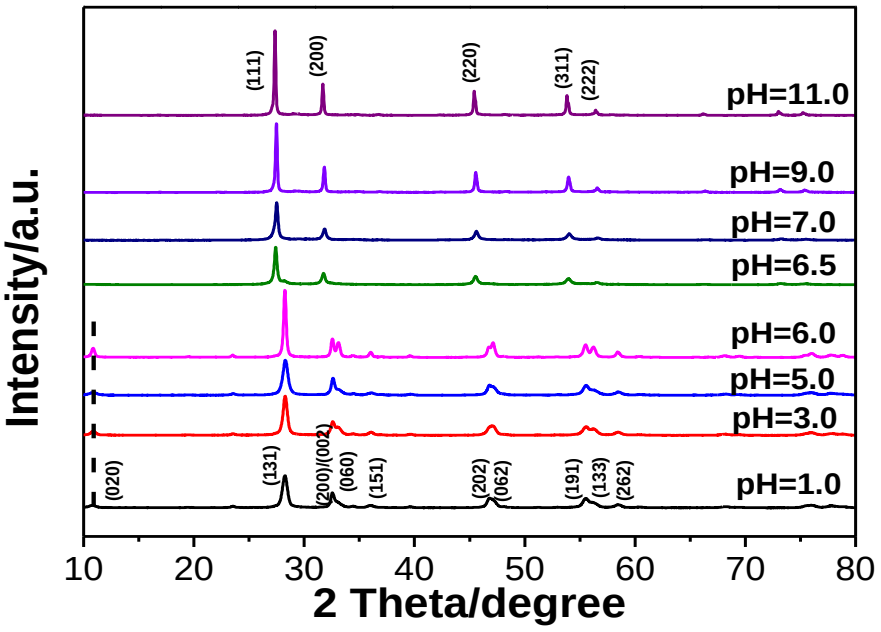

Fig. 1. XRD patterns of bismuth molybdate prepared at the different pH.

Fig. 2 show the SEM images of the as-synthesized bismuth molybdate samples at different pH values. As can be seen, pH significantly influences the morphologies of

bismuth molybdate samples. Under acidic condition (pH ≤ 6.0), all Bi_2MoO_6 crystals reveal the irregular sheet-shaped structure with the thickness of several nanometers. With the pH increasing from the 1.0 to 6.0, the as-obtained Bi_2MoO_6 nanosheets grow gradually with the width from 63 nm to 234 nm and the thicknesses from 16 nm to 35 nm. When the pH is 6.5 (Fig. 2 E), many irregular nanoparticles with diameter from a few nanometer to tens of nanometer appear, coexisting with a small amount of nanosheets. These nanoparticles agglomerate together to form the big spherical agglomerates. At pH 7.0 (Fig. 2 F), the nanoparticles become bigger and the nanowires appear. With pH increasing from 7.0 to 11.0 (Fig. 3 F-H), the size of nanoparticles and the length of nanowires gradually increase. Furthermore, under alkaline condition (pH 9.0 and 11.0), the bismuth molybdate nanoparticles become more irregular and exhibit diamond shape.

TEM images of bismuth molybdate samples obtained at different pH are showed in Fig. 3 A−H. Under acidic condition (pH 1.0, pH 3.0, pH 5.0 and pH 6.0), all Bi_2MoO_6 crystals exhibit sheet-shaped structure, and the plate size increases from 40 nm to 200 nm with the pH from pH 1.0 to pH 6.0 (Fig. 3 A to D), which is in agreement with the SEM characterization. When the pH is 6.5 (Fig. 3 E), it seems that many small Bi_2O_3 nanoparticles with size of a few nanometer to tens of nanometer grow on the surface of some large partilces. With pH from the 7.0 to 11.0, these spherical nanopartilces gradually grow into the diamond-like bismuth molybdate particles coexisting with many nanowires, and the average size of these spherical nanopartilces increases from 50 nm to 200 nm.

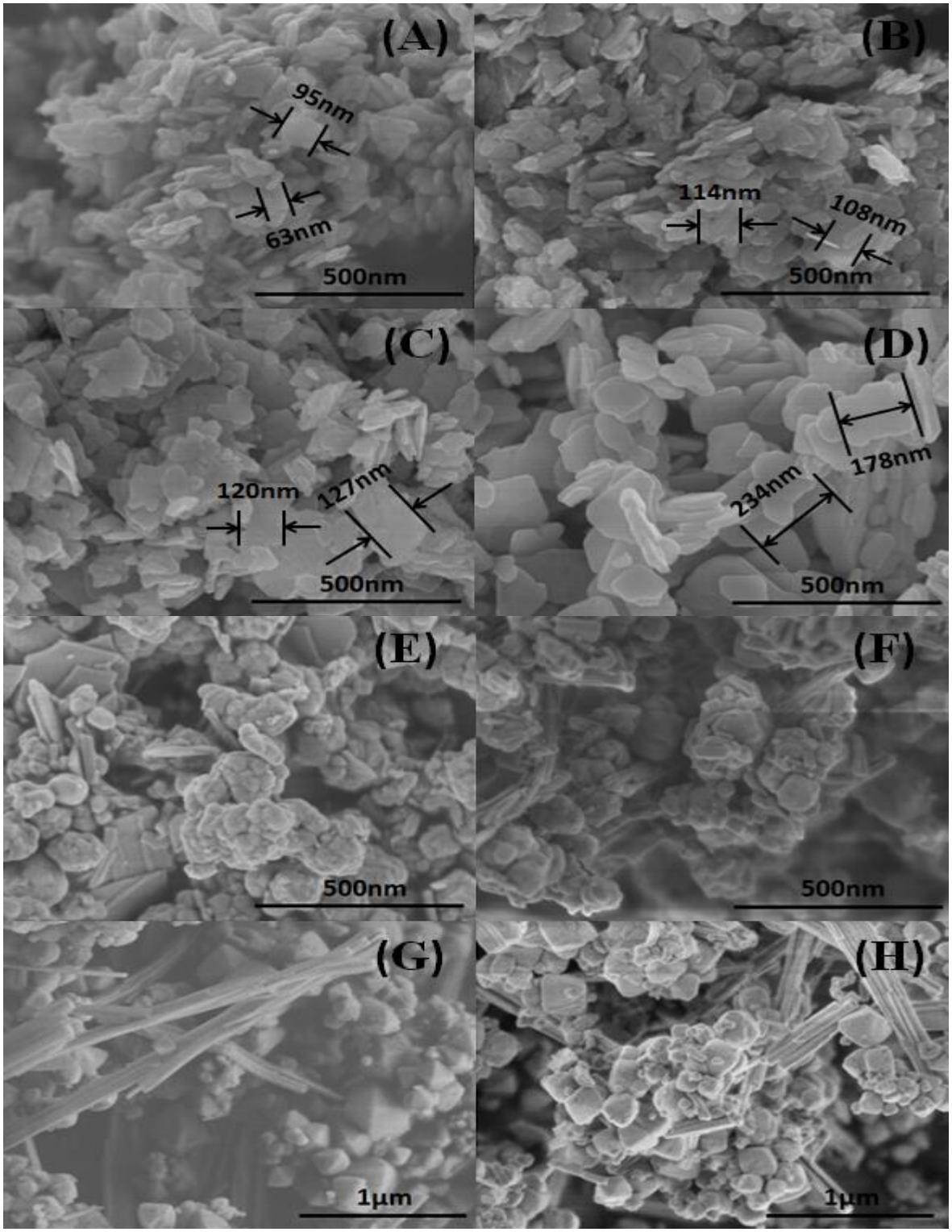

Fig. 2. SEM images of bismuth molybdate samples obtained at different pH. A: pH1.0, B: pH 3.0, C: pH 5.0, D: pH 6.0, E: pH 6.5, F: pH 7.0, G: pH 9.0, H: pH 11.0.

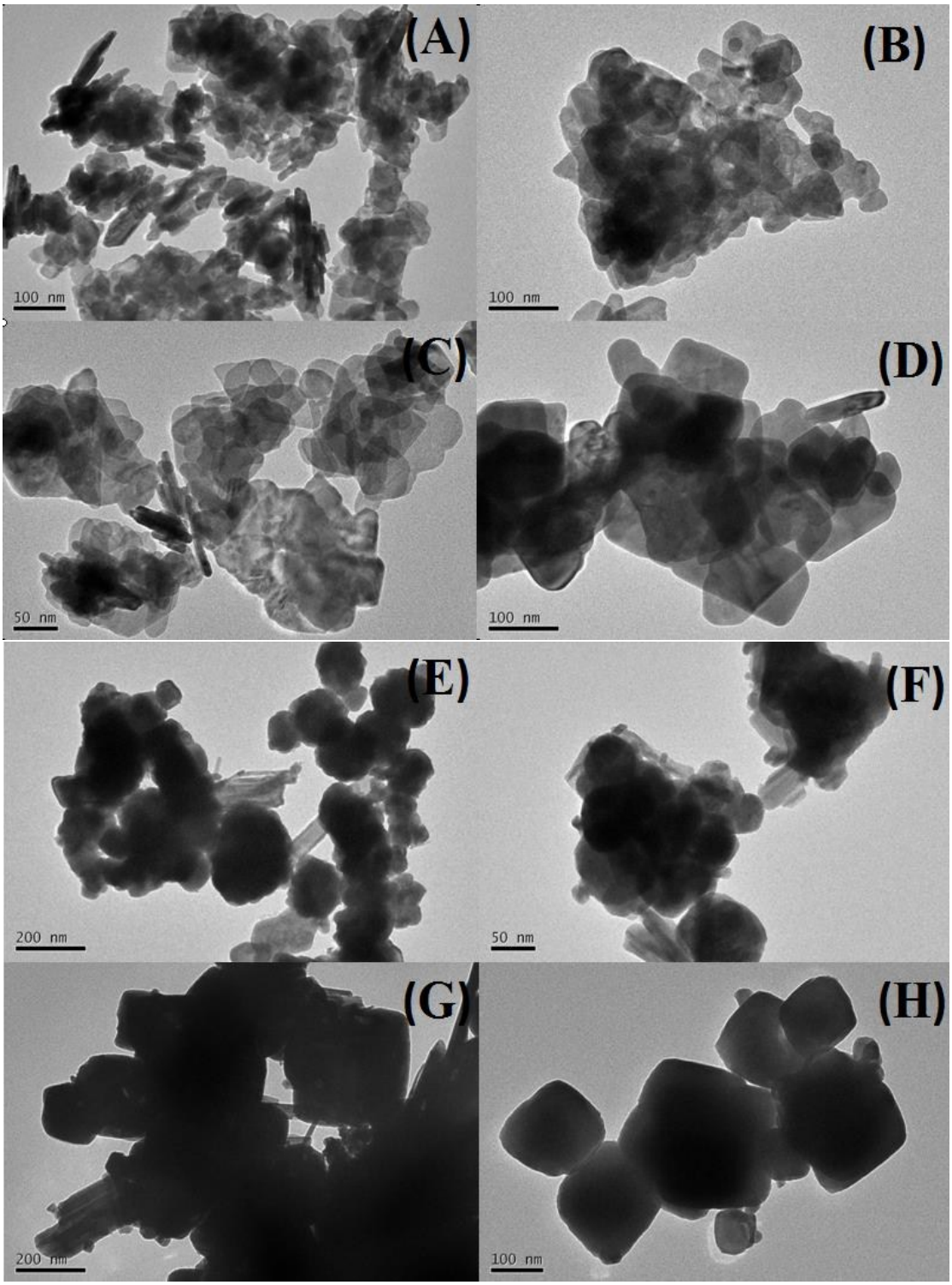

Fig. 3. TEM images of bismuth molybdate samples obtained at different pH. A: pH1.0, B: pH 3.0, C: pH 5.0, D: pH 6.0, E: pH 6.5, F: pH 7.0, G: pH 9.0, H: pH 11.0

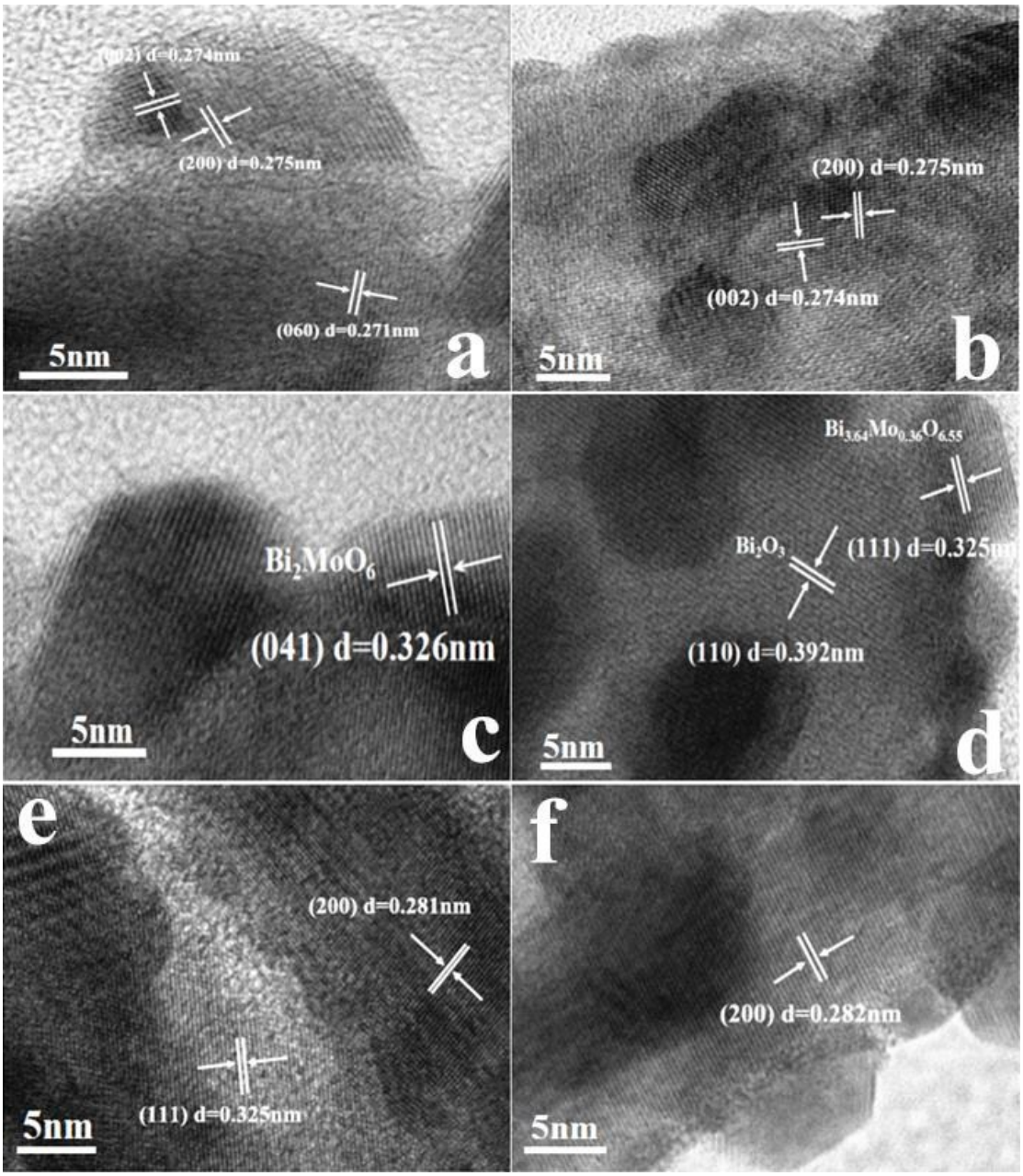

Fig. 4. HTEM images of bismuth molybdate samples obtained at different pH. A: pH 3.0, B: pH 5.0, C: pH 6.0, D: pH 6.5, E: pH 7.0, F: pH 9.0

HRTEM images of the bismuth molybdate samples prepared at different pH are given in Fig. 4. The interlayer spacing of 0.274 nm, 0.275 nm and 0.326 nm corresponding to (0 0 2), (2 0 0) and (0 4 1) crystal planes of orthorhombic Bi_2MoO_6 can be observed in the sample prepared at pH 3.0 (Fig. 4A), pH 5.0(Fig. 4B) and pH 6.0(Fig. 4C), respectively. When the pH value is 6.5 (Fig. 4D), the d spacing of 0.39

nm and 0.33 nm correspond to the lattice spacing of (1 1 0) and (1 1 1) crystal plane of Bi_2O_3 and $Bi_{3.64}Mo_{0.36}O_{6.55}$, respectively, showing that the new phases of Bi_2O_3 and $Bi_{3.64}Mo_{0.36}O_{6.55}$ were formed. For the sample prepared under basic condition (Fig. 4E and 4F), the d spacing of 0.281 nm and 0.325 nm corresponding to (2 0 0) and (1 1 1) crystal planes of cubic $Bi_{3.64}Mo_{0.36}O_{6.55}$ phase can be observed, revealing that phase transformation of bismuth molybdate can be happened by controlling the pH value in the reaction system. The phase transformation of bismuth molybdate agrees well with the XRD result.

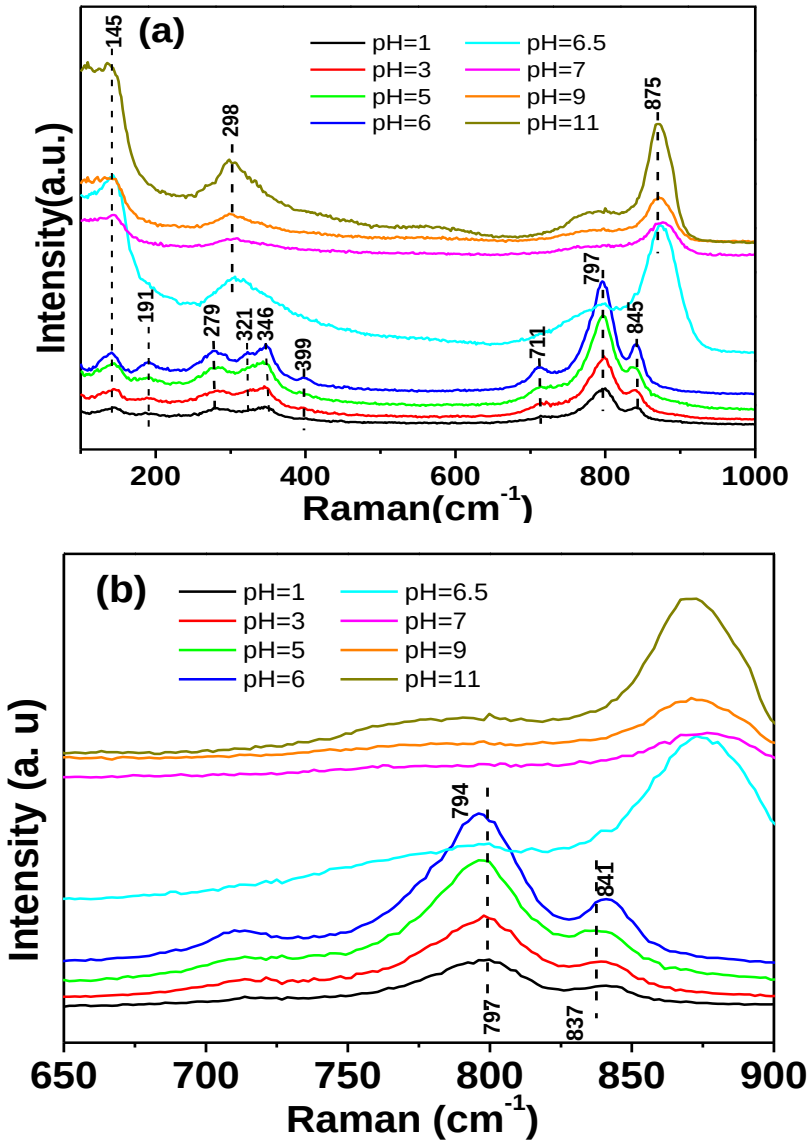

Fig. 5. Raman spectra of the bismuth molybdate samples obtained at different pH (a) and the partial enlarged detail of Raman spectra (b).

Raman spectroscopy is effective to probe the local structure of materials because the Raman spectrum reflects the bonding states in the coordination polyhedra of a material. Raman spectra of the bismuth molybdate samples obtained at different pH value were recorded at room temperature and depicted in Fig. 5. Generally, the Raman modes at 841 cm^{-1}(w, sh), 797 cm^{-1}(vs), 711 cm^{-1}(m), 399 cm^{-1}(m), 346 cm^{-1}(s), 321 cm^{-1}(w), 279 cm^{-1}(s), 191 cm^{-1}(m), 145 cm^{-1}(m) are assigned to the stretching vibrations of the characteristic peaks of Bi_2MoO_6 (Fig. 5a). The modes near 321 cm^{-1}, 346 cm^{-1} and 399 cm^{-1} correspond to the Eu symmetry bending modes of MoO_6 octahedra, and the Raman modes near 279 cm^{-1} originate most likely from the Eg mode bending vibration of MoO_6 octahedra.[17] All samples have the band at 145 cm^{-1} which is assigned to the lattice modes of Bi^{3+} atoms mainly in the direction perpendicular to the layers. The bismuth molybdate samples prepared at pH 1.0, pH 3.0, pH 5.0 and pH 6.0 have the similar Raman vibration modes of Bi_2MoO_6 phase (Fig. 5a). While when the pH > 6.0, the characteristic Raman vibration modes of MoO_6 octahedra disappear and two new peaks at 875 cm^{-1}, 298 cm^{-1} appear, indicating that the structure of orthorhombic Bi_2MoO_6 was destroyed and a new phase of cubic $Bi_{3.64}Mo_{0.36}O_{6.55}$ formed. The changes of Raman vibration modes with pH suggest that the pH value can control the phase transformation of bismuth molybdate. It has been reported that Raman modes mainly at 797cm^{-1} (A1g mode) and 845cm^{-1} (A2u mode) can be assigned to the symmetric and asymmetric stretching vibrations of the MoO_6 octahedra that involve motions of the apical oxygen atoms which are

perpendicular to the layers.[10] Variations in the width and the relative position of these two bands suggested that the stretching modes of the Mo-O bond are different. As showed in Fig. 5b, with the pH increasing from 1.0 to 6.0, the strong band at 797cm^{-1} and 837 cm^{-1} was found to be shifted to 794 cm^{-1} and 841 cm^{-1}, respectively. The minute shift in position suggests that there might be some subtle rearrangements in the structure [25] and confirms that the pH value in the reaction system could result in the structure change of MoO_6 octahedron related to the apical oxygen atoms. This fact agrees with the SEM and TEM results that the thickness of Bi_2MoO_6 nanosheet gradually becomes large with the increase of pH value from 1.0 to 6.0. Meanwhile, the Raman band intensity increases with the pH due to the increase of crystallinity.

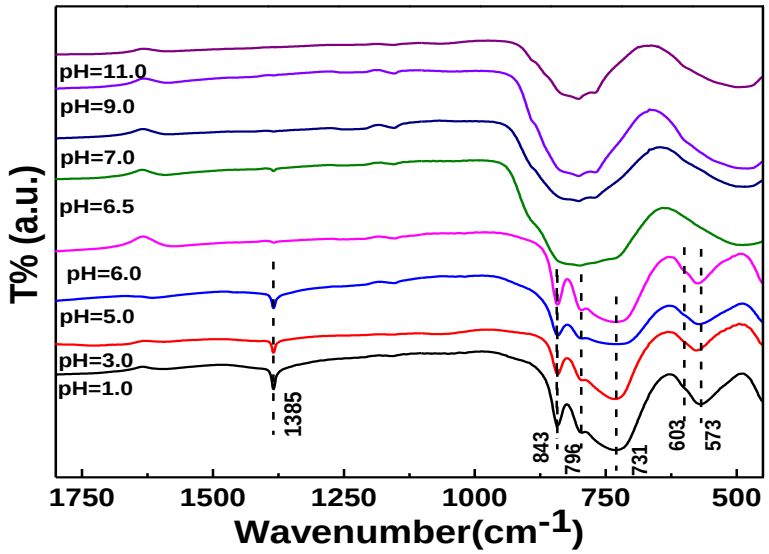

Fig. 6. FT-IR spectra of bismuth molybdate samples obtained at different pH.

Fig. 6 shows FT-IR spectra of Bi_2MoO_6 samples obtained at different pH. Two regions can be observed: one in the 950-700 cm^{-1} range, where the Mo-O stretching bands are recorded, and the other in the 600-450 cm^{-1} range, corresponds to stretching and deformation modes involving Bi-O modes.[24-26] The bands at around 843 and 796

cm^{-1} can be assigned as the asymmetric and symmetric stretching modes of MoO_6 involving vibrations of the apical oxygen atoms, respectively. The band at 731cm^{-1} is attributed to the asymmetric stretching mode of MoO_6 involving vibrations of the equatorial oxygen atoms and the bands at 603, 573 cm^{-1} correspond to the bending vibration of MoO_6.[10] All the characteristic absorption band of MoO_6 disappear and a broad absorption band between 720 and 850 occurs when the pH $\geq$ 6.5. This phenomenon means that the MoO_6 octahedron structure was completely destroyed and a new structure of bismuth molybdate phase has formed. It should be noted that an obviously absorption peak at 1385 cm^{-1}, which is assigned to the vibration of NO_3^-, can be observed by the samples prepared at pH 1.0, pH 3.0 and pH 5.0. Furthermore, the intensity of this peak decreases with the pH form 1.0 to 5.0, and almost disappears under pH 6.0. This means that these sample might contain a small amount of hydrolysis products such as $BiONO_3$ or $Bi_2O_2(OH)NO_3$. This fact also indicates that parts of $BiONO_3$ and $Bi_2O_2(OH)NO_3$ did not participate in the reaction of Bi_2MoO_6 formation because the hydrolysis reaction was inhibited to some extend under the strong acidic condition. The disappearance of the absorption peak at 1385 cm^{-1} at pH 6.0 means that most of $BiONO_3$ and $Bi_2O_2(OH)NO_3$ have engaged in the reaction, and suggests that the increase in pH can promote the hydrolysis reaction and the growth of Bi_2MoO_6 crystal. This phenomenon is consistent with the XRD result that the crystallinity of Bi_2MoO_6 crystal increased with pH.

3.2 Formation mechanism of bismuth molybdate nanostructure

In generally, the shape of the nanostructures is strongly dependent on the relative

chemical potential. It has been reported that orthorhombic Bi_2MoO_6 is constructed by a corner-shared MoO_6 octahedral layer and $[Bi_2O_2]^{2+}$ atom layers sandwiched between MoO_6 octahedral layers. On the basis of Bi_2MoO_6 structure, the facets which are perpendicular to the chains of octahedral-Mo usually have a much higher chemical potential in comparison with other facets. Thus the crystal growth was preferentially along the layer. Under a low pH condition (pH ≤ 6.0), there would be abundant H^+ in the system to adsorb on the (0 1 0) crystal planes and even on (0 0 1) and (1 0 0) planes because of the high density of oxygen atoms on (0 1 0) planes, leading to remarkable reduction of surface energy of (1 0 0) planes. Therefore, it is possible to form a relatively thin layer along [0 1 0] direction.[27] It can be seen that all samples prepared under the acidic condition exhibit nanosheet-shaped structure. With the increase of pH from the 1.0 to 6.0, both the length and the thickness of these Bi_2MoO_6 nanosheets become large. However, when pH in solution is higher than 6.5, the H^+ concentration sharply decreases, causing the surface free energies of the various crystallographic planes change significantly. The surface energy of these planes which have the dominant adsorption of OH^- would decrease, thus slowing down the growth of those facets. Subsequently, the enlargement in a, b planes was prohibited, and the growth rate of nuclei along the directions of [0 1 0] increases. It is important that the change of growth rate for the various crystallographic planes promotes the formation of the new phases of Bi_2O_3 and cubic $Bi_{3.64}Mo_{0.36}O_{6.55}$. This fact is confirmed by XRD, TEM and Raman result. Under alkaline condition (pH ≥ 6.5), the Bi_2MoO_6 nanosheets disappears. With further increasing the pH value, the Bi_2O_3

nanoparticle firstly appears, and finally completely transformed to the cubic $Bi_{3.64}Mo_{0.36}O_{6.55}$ phase with spherical-shaped structure. Therefore, pH significantly influences the morphologies and phase structure of the bismuth molybdate products.

The remarkably distinct morphologies and phase structures of the bismuth molybdate products at different pH are determined by the transformations of Bi and Mo resources. It is well known that $Bi(NO_3)_3 \cdot 2H_2O$, a strong-acid weak-base salt, ionize into Bi^{3+} and NO_3^{-1} (Eq. 1) in strong acid solution or hydrolyzes in water to yield $BiONO_3$ (Eq. 2) , which would converted to $Bi_2O_2(OH)NO_3$ (Eq. 3) and Bi_2O_3 (Eq. 4) in weak acidic solution. The appearance of $BiONO_3$ and $Bi_2O_2(OH)NO_3$ hydrolysis products at the pH ≤ 6.0 is confirmed by FI-IR. Those hydrolysis products would react with MoO_4^{2-} to obtain an amorphous Bi_2MoO_6. Subsequently, the amorphous Bi_2MoO_6 gradually transforms into orthorhombic Bi_2MoO_6 through the refluxing reaction (Eq. 5-8). When pH in the reaction solution is higher than 6.5, the Bi_2O_3 nanoparticles formed, which reacts with MoO_4^{2-} or amorphous Bi_2MoO_6 to obtain a cubic $Bi_{3.64}Mo_{0.36}O_{6.55}$ phase through the refluxing method (Eq. 9-11).

The formation of Bi resources:

$$Bi(NO_3)_3 \Leftrightarrow Bi^{3+} + 3NO_3^{3-} \quad (1)$$

$$Bi^{3+} + 3NO_3^- + H_2O \Leftrightarrow BiONO_3 + 2H^+ + 2NO_3^- \quad (2)$$

$$2BiONO_3 + H_2O \Leftrightarrow Bi_2O_2(OH)NO_3 + H^+ + NO_3^- \quad (3)$$

$$Bi_2O_2(OH)NO_3 + OH^- \Leftrightarrow Bi_2O_3 + H_2O + NO_3^- \quad (4)$$

The formation of orthorhombic Bi_2MoO_6 phase at pH ≤ 6.0

$$BiONO_3 \Leftrightarrow BiO^+ + NO_3^- \quad (5)$$

$$Bi_2O_2(OH)NO_3 \Leftrightarrow Bi_2O_2^{2+} + OH^- + NO_3^- \quad (6)$$

$$2BiO^+ + MoO_4^{2-} \xrightarrow{\text{Reflux reaction}} Bi_2MoO_6\ (\text{orthorhombic}) \quad (7)$$

$$Bi_2O_2^{2+} + MoO_4^{2-} \xrightarrow{\text{Reflux reaction}} Bi_2MoO_6\ (\text{orthorhombic}) \quad (8)$$

The formation of cubic $Bi_{3.64}Mo_{0.36}O_{6.55}$ phase at pH ≥ 6.5

$$Bi_2O_2^{2+}(2BiO^+) + MoO_4^{2-} \Leftrightarrow Bi_2MoO_6\ (\text{amorphous}) \quad (9)$$

$$Bi_2MoO_6(amorphous) + Bi_2O_3 \xrightarrow{\text{Reflux reaction}} Bi_{3.64}Mo_{0.36}O_{6.55}\ (\text{cubic}) \quad (10)$$

$$Bi_2O_3 + MoO_4^{2-} \xrightarrow{\text{Reflux reaction}} Bi_{3.64}Mo_{0.36}O_{6.55}\ (\text{cubic}) \quad (11)$$

3.3 Photocatalytic performances and mechanism for the visible-light photoactivity enhancement

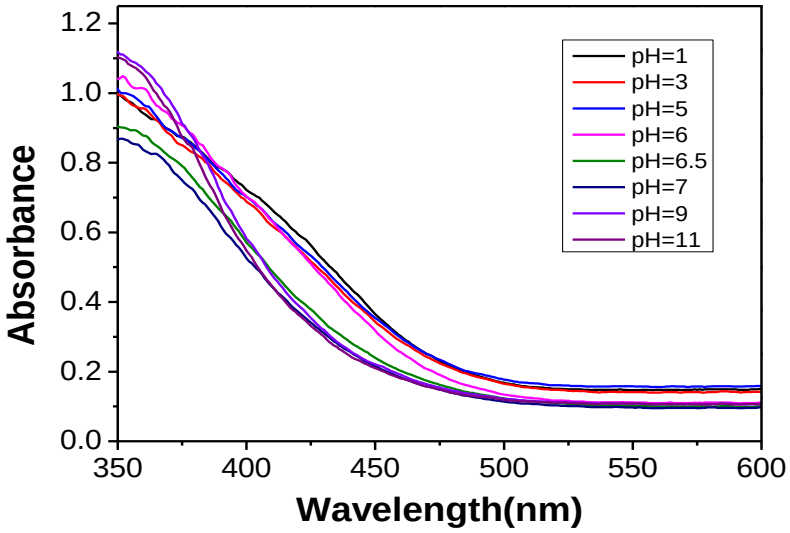

Fig. 7. UV–vis diffuse reflectance spectra of bismuth molybdate samples obtained at different pH.

UV-DRS spectra of the bismuth molybdate samples obtained at different pH are shown in Fig. 7. All the products exhibit absorption bands in the visible light region, which represent the characteristic absorption of bismuth molybdate samples. As expected, bismuth molybdate samples prepared under acidic condition (pH 1.0 to pH 6.0) almost have the same fundamental absorption edge with the Bi_2MoO_6. With the

increase of the pH from 1.0 to pH 6.0, the absorption edge decrease from 480 nm to 476 nm (band gap from 2.58 eV to 2.60 eV), suggesting only a little blue shift of absorption edge with pH. However, after the pH exceeds 6.0, the absorption edge has a large blue shift. At pH 6.5, pH 7.0, pH 9.0 and pH 11.0, the absorption edge is 457 nm, 452 nm, 432 nm and 428 nm, respectively. This fact suggests that the formation of $Bi_{3.64}Mo_{0.36}O_{6.55}$ phase has a larger band gap compared with that of Bi_2MoO_6. The reduction of the visible-light absorption might be the one of the direct reason for the lower visible-light photoactivity of $Bi_{3.64}Mo_{0.36}O_{6.55}$ than that of Bi_2MoO_6.

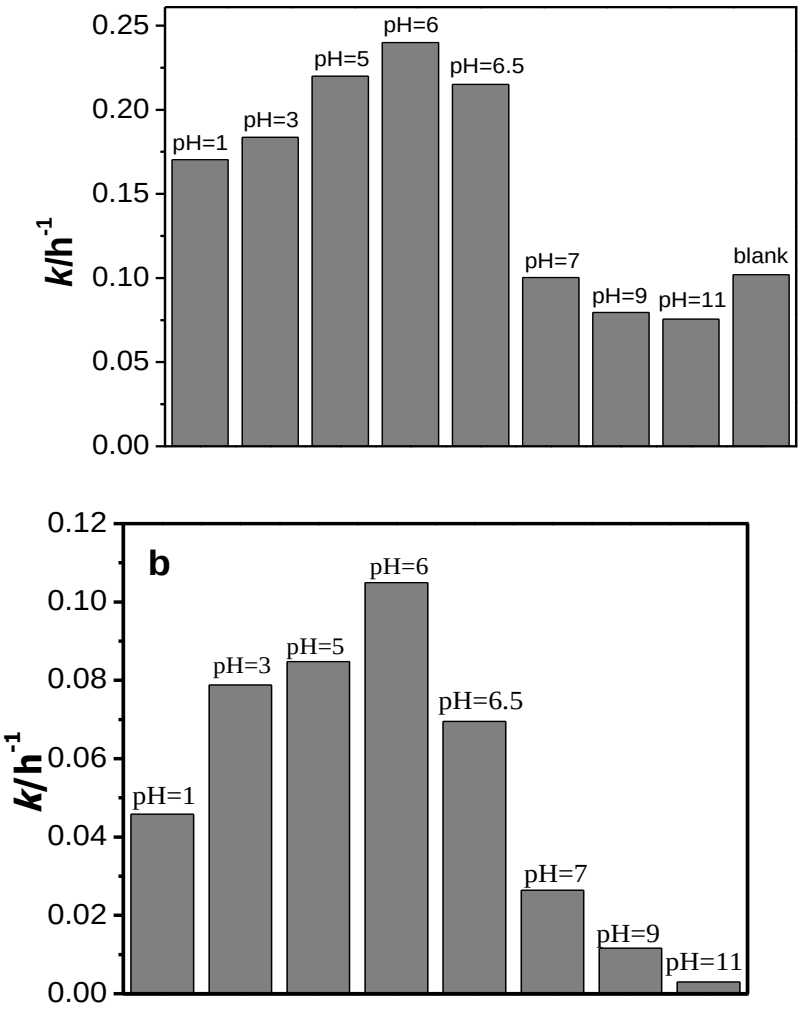

Fig.8. Apparent rate constants for the photocatalytic degradation of MB (a) and MO (b) over the samples obtained at different pH values under visible light irradiation (λ > 420 nm).

Fig. 8 displays the apparent rate constants for the photocatalytic degradation of MB (Fig. 8a) and MO (Fig. 8b) over the samples obtained at different pH under visible light irradiation ($\lambda > 420$ nm). The blank experiment without the catalyst under same condition was done to show the self-degradation of dye. Fig. 8a shows that the self-degradation of MB is a little higher than MB degradation over the samples under 9 and 11. One reason is that the experimental error exists among the different experimental test. Another reason is that the catalyst in dye solution would shade off the light, resulting in the decrease of the dye self-degradation. In Fig. 8a, the photocatalytic activity of Bi_2MoO_6 sample for MB degradation increases with the pH from 1.0 to 6.0, and the sample obtained at pH 6.0 exhibited the best photocatalytic activity. The reason might be the increase in the crystallinity of Bi_2MoO_6 with pH value in the synthesis reaction system. After the pH exceeds 6.0, the photocatalytic activity sharply decreases. Fig. 8b shows the photocatalytic performances of the different Bi_2MoO_6 samples for MO degradation. The trend of photocatalytic activity of MO degradation over the Bi_2MoO_6 samples is the same with that of MB degradation. The Bi_2MoO_6 sample obtained at pH 6.0 exhibits the best photocatalytic activity for MO degradation, and the samples prepared under the acidity condition have better photocatalytic activity than those prepared under the alkalinity condition. These results confirm that the Bi_2MoO_6 nanosheets had superior photocatalytic activities compared with the $Bi_{3.64}Mo_{0.36}O_{6.55}$ nanoparticles. The higher photocatalytic activity can be explained by the two reasons: one possible reason is that the thin nanosheets results in a relatively large distortion of the unit cell due to the large

surface strain, and the nanosheet structure are helpful for the electron–holes generated inside the crystal to transfer to the surface and then react with MB. The other reason is that the band gaps of the Bi_2MoO_6 samples are much lower than those of $Bi_{3.64}Mo_{0.36}O_{6.55}$ samples, which means the higher visible light absorption ability.

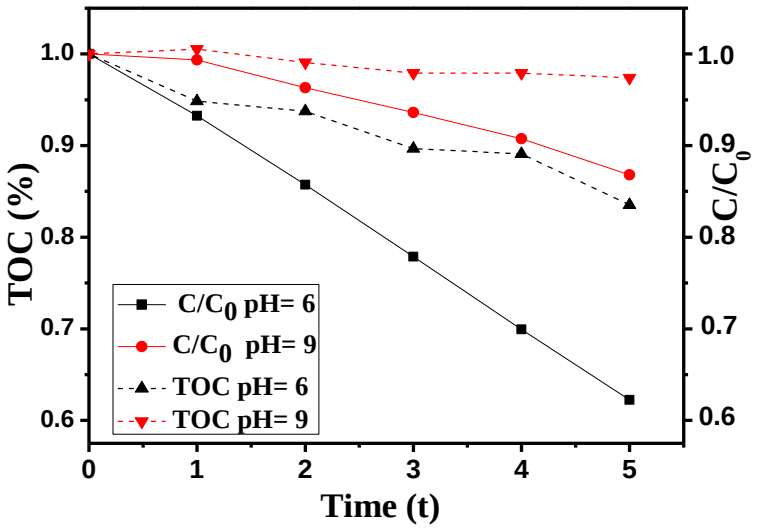

Fig.9. The change of TOC and MB concentration in solution for the photocatalytic degradation of MB over the Bi_2MoO_6 samples at pH 6.0 and pH 9.0 under visible light irradiation ($\lambda > 420$ nm).

To further investigate the mineralization properties of the Bi_2MoO_6 samples, the total organic carbon (TOC) in the MB solution was determined, as shown in Fig. 9. The TOC removal efficiency is consistent with the MB photodegradation activity. After 5 h the photodegradation reaction, the percentages of concentration decrease are 38% and 24%, and the TOC removal efficiencies are 17% and 6% over the Bi_2MoO_6 samples at pH 6.0 and pH 9.0, respectively. This fact shows that not all MB was mineralized in to CO_2, and parts of MB were changed into the intermediate products. The TOC removal efficiency of the Bi_2MoO_6 sample at pH 6.0 is higher that that of the Bi_2MoO_6 sample at pH 9.0, suggesting that the Bi_2MoO_6 sample at pH 6.0 have the better mineralization ability than the sample at pH 9.0.

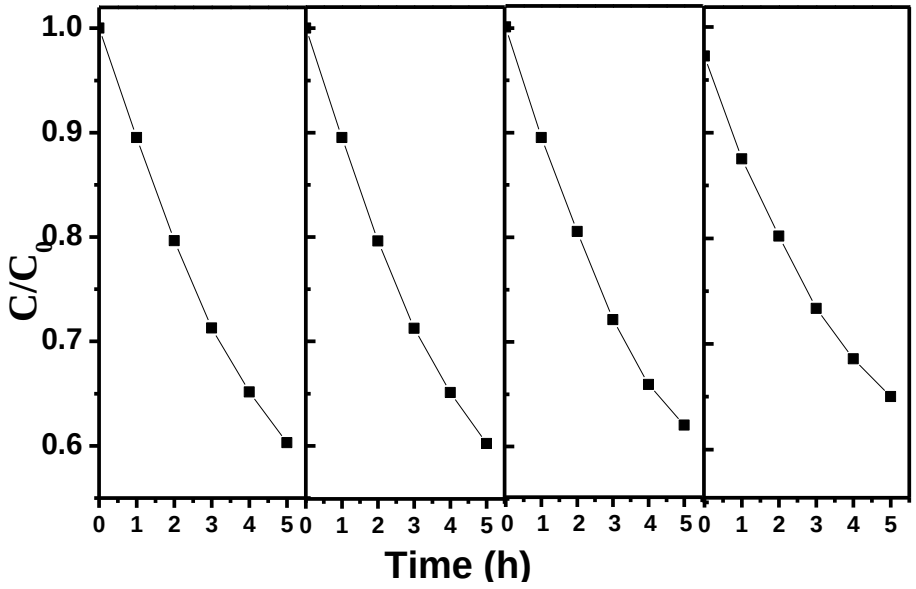

Fig. 10. The cycling photocatalytic performance of the Bi_2MoO_6 sample (pH = 6.0) for MB degradation.

Long-term stability of a photocatalyst during reaction is necessary to evaluate for the practical applications. Stability tests were therefore performed by executing recycling reactions four times for the photodegradation of MB over the Bi_2MoO_6 sample (pH 6.0) under visible light irradiation (Fig.10). As shown in Fig.10, no obvious loss of the photocatalytic activity of the Bi_2MoO_6 sample (pH 6.0) was observed for MB degadation after four cycles, suggesting that this Bi_2MoO_6 catalyst is stable during the reaction.

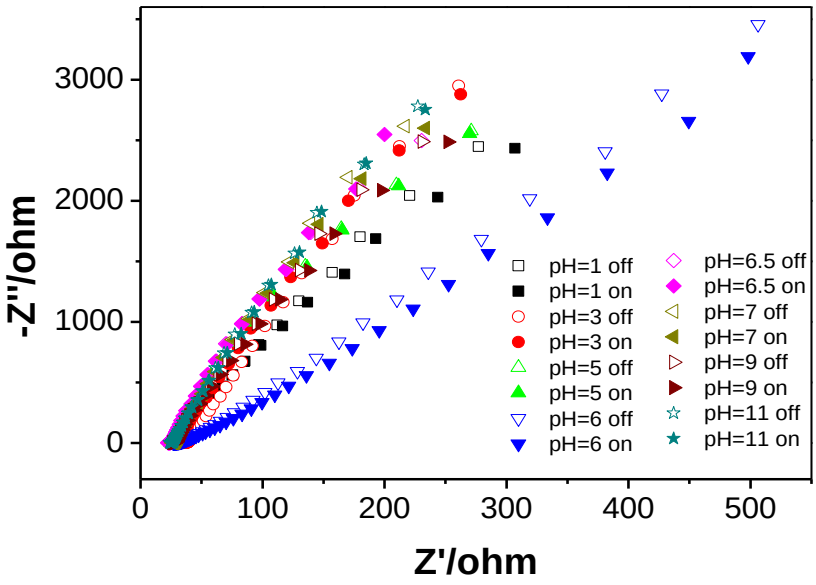

Fig. 11. Nyquist plots for the bismuth molybdate samples under visible light illumination [Na_2SO_4 = 0.1 M].

The interface charge separation efficiency of photogenerated electrons and holes was investigated by the typical EIS (presented as Nyquist plots). The radius of the arc on the EIS spectra reflects the interface layer resistance occurring at the surface of electrode. The smaller arc radius implies higher efficiency of charge transfer.[28] Fig. 11 gives the EIS Nyquist plots for the Bi_2MoO_6 samples obtained at different pH in aqueous solution under visible light illumination. The arc radius of the samples obtained under acidic condition is smaller than those of the samples under alkaline conditions. Obviously, when the pH is 6.0, the arc radius of the sample is the smallest, demonstrating that there is the best separation and transfer efficiency of the photogenerated electron-hole pairs. The tendency of the EIS spectra is consistent with that of photocatalytic activities of the bismuth molybdate samples. The high photocatalytic activities for the Bi_2MoO_6 might be that the thin nanosheet structure is helpful for the transfer of the electron-hole pairs because the photogenerated electrons and holes can transfer to the surface of the catalyst through the relatively shorter

distance compared with the samples with the spherical structure.

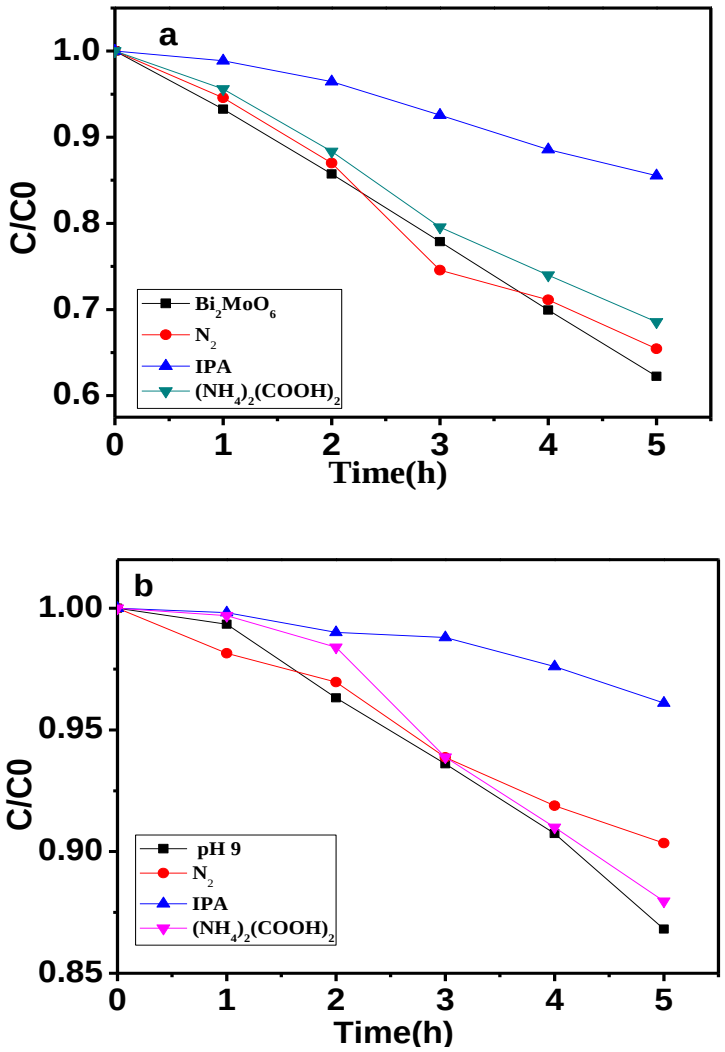

Fig. 12. Plots of photogenerated carriers trapping in the system of photodegradation of MB under visible light by (a) Bi_2MoO_6 (pH =6.0) and (b) $Bi_{3.64}Mo_{0.36}O_{6.55}$ (pH =9.0).

The main oxidative species could be detected by the trapping experiments of active species, using $(NH_4)_2C_2O_4{\cdot}H_2O$ as the hole scavenger and t-BuOH as the hydroxyl radical scavenger. N_2 was used to avoid the formation of he $\bullet O_2^-$ radical scavenger. As shown in Fig. 12a and 11b, the photocatalytic degradation efficiencies of MB over Bi_2MoO_6 and $Bi_{3.64}\ Mo_{0.36}\ O_{6.55}$ significantly decrease in the presence of 1 mM $(NH_4)_2C_2O_4{\cdot}H_2O$, while there is only little change for the photocatalytic degradation efficiencies by adding the t-BuOH or purging N_2 in the system. This fact

shows that photo-generated holes were the major oxidative species for the Bi_2MoO_6 and $Bi_{3.64}Mo_{0.36}O_{6.5}$, while the hydroxyl radical and $\bullet O_2^-$ radical have little effect on the photodegradation of MB. The trapping experiments of active species were also carried out during MO degradation to further confirm that the photo-generated holes were the major oxidative species for the Bi_2MoO_6 and $Bi_{3.64}Mo_{0.36}O_{6.5}$, and the hydroxyl radical and $\bullet O_2^-$ radical have little effect on the photodegradation of MO (Fig. S1). This fact is agreement with that of the MB degradation.

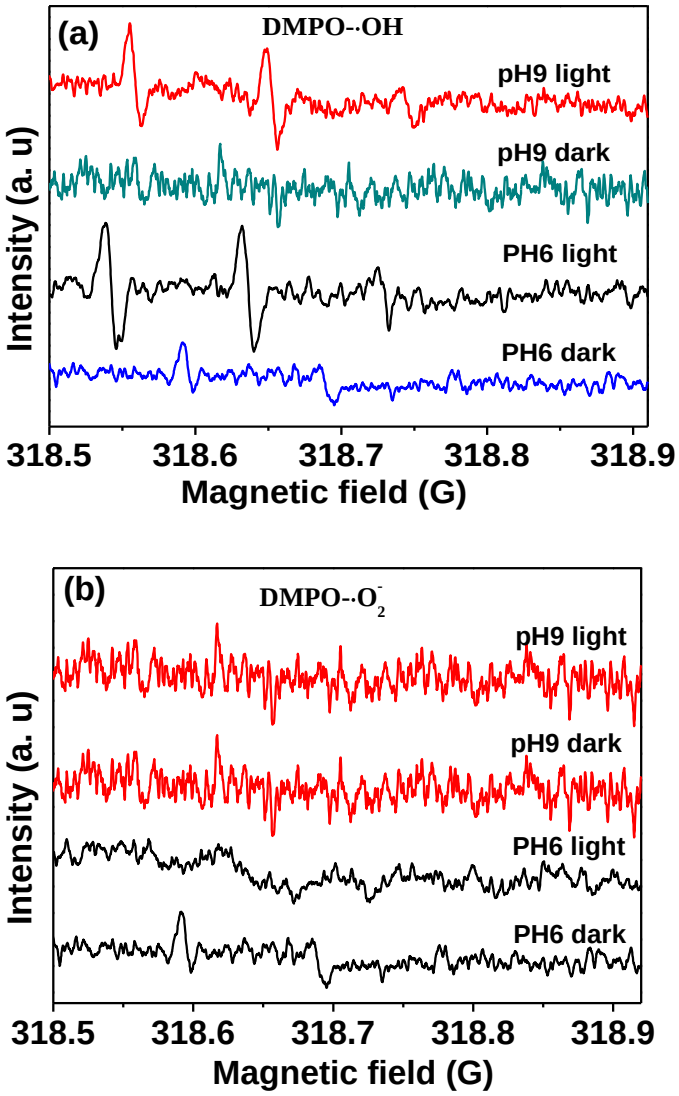

Fig. 13. ESR spectra of (a) Bi_2MoO_6 (pH = 6.0) and $Bi_{3.64}Mo_{0.36}O_{6.55}$ (pH= 9.0) sample in water and (b). Bi_2MoO_6 (pH = 6.0) and $Bi_{3.64}Mo_{0.36}O_{6.55}$ (pH=9.0) sample in DMSO

ESR is a useful tool to monitor main oxidative specie. DMPO (5,5-dimethyl-1-pyrroline N-oxide) is nitrone spin trap generally used for trapping radicals due to the generation of stable free radicals, DMPO-•OH or DMPO-•O_2^-. Fig. 13a shows the signals of the DMPO-•OH adduct for Bi_2MoO_6 (pH=6.0) and $Bi_{3.64}Mo_{0.36}O_{6.55}$ (pH=9.0). The DMPO-•OH signals of both the two samples have the typical hydroxyl radicals quad peaks, indicating hydroxyl radicals are engaged in the photocatalytic process. Obviously, the overall signal intensity of Bi_2MoO_6 (pH=6.0) is higher than that of the $Bi_{3.64}Mo_{0.36}O_{6.55}$ (pH=9.0), suggesting that more hydroxyl radicals are produced during the reaction. This is direct reason that Bi_2MoO_6 (pH=6.0) has the higher photocatalytic activity than that of the $Bi_{3.64}Mo_{0.36}O_{6.55}$ (pH=9.0). Fig. 13b shows that the DMPO-•O_2^- signals in with dimethyl sulphoxide (DMSO) as the solvent instead of water. It is seen that no •O_2^- signals can be detected, suggesting that •O_2^- hardly has any effect on the photodegradation of MB. Therefore, the ESR results show that •OH is major oxidative specie of Bi_2MoO_6 and $Bi_{3.64}Mo_{0.36}O_{6.55}$ for the MB degradation, which is in agreement with the trapping experiments of active species.

4. Conclusions

The bismuth molybdates with the different phase structures and morphologies were controllably synthesized through the refluxing method by adjusting the pH in the reaction system. The Bi_2MoO_6 nanosheets were easily obtained under the acidic condition (pH $\leq$ 6.0), while $Bi_{3.64}Mo_{0.36}O_{6.55}$ nanoparticles were formed under the circumneutral and basic condition (pH $\geq$ 6.5). The main reasons for the phase

structure and morphology transformation of these two bismuth molybdates are due to modulating the kinetics of nucleation and growth of the crystal by the preferential adsorption of H^+ onto different crystal facets and to the hydrolysis products such as $BiONO_3$, $Bi_2O_2(OH)NO_3$ and Bi_2O_3 as initial seeds by tuning the pH value in the reaction system. The Bi_2MoO_6 nanosheet has the higher visible light photocatlaytic activity than $Bi_{3.64}Mo_{0.36}O_{6.55}$ nanoparticle due to the nanosheet structure and the relative narrow band gap. The Bi_2MoO_6 nanosheet prepared under pH 6.0 has the highest photocatalytic acitivity. The species trapping and ESR experiments showed that both Bi_2MoO_6 and $Bi_{3.64}Mo_{0.36}O_{6.55}$ have the same photocatalytic mechanism and the main active species for the MB degradation is hydroxyl radical.

Acknowledgement

This present work is supported by the National Natural Science Foundations of China (Grant No. 21577132), the Fundamental Research Funds for the Central Universities (Grant No. 2652015225), National High Technology Research and Development Program of China (2012AA062701).

Reference

1. D. Kannaiyan, E. Kim, N. Won, K. W. Kim, Y. H. Jang, M.-A. Cha, D. Y. Ryu, S. Kim and D. H. Kim, *J. Mater. Chem.*, 2010, 20, 677-682.

2. G. H. Tian, H. G. Fu, L. Q. Jing, B. F. Xin and K. Pan, *J. Phys. Chem. C*, 2008, 112, 3083-3087.

3. S. Tokunaga, H. Kato and A. Kudo, *Chem. Mater.*, 2001, 13, 4624-4628.

4. S. Murugesan and V. (Ravi) Subramanian, *Chem. Commun.*, 2009, 34,

5109-5111.

5. Y. Hou, X. Y. Li, Q. D. Zha and G. H. Chen, *Appl. Cataly. B: Environ.*, 2013, 142–143, 80–88.

6. L. W. Zhang, Y. J. Wang, H. Y. Cheng, W. Q. Yao and Y. F. Zhu, *Adv. Mater.*, 2009, 21, 1286-1297.

7. G. H. Tian, Y. J. Chen, W. Zhou, K. Pan, Y. Z. Dong, C. G. Tian and H. G. Fu, *J. Mater. Chem.*, 2011,21, 887-892.

8. Y. Shimodaira, H. Kato, H. Kobayashi and A. Kudo, *J. Phys. Chem. B*, 2006, 110, 17790-17797.

9. T. X. Liu, B. X. Li, Y.G. Hao and Z.Y. Yao, *Chem. Eng. J.*, 2014, 244, 382-390.

10. Y. Shimodaira, H. Kato, H. Kobayashi and A. Kudo, *J. Phy.Chem*. B, 2006, 110, 17790-17797.

11. J. Ren, W. Wang, M. Shang, S. Sun and E. Gao, *ACS Appl. Mater. Interfaces*, 2011, 3, 2529-2533.

12. J. Zou, J. Ma, Q. Huang, S. Luo, J. Yu, X. Luo, W. Dai, J. Sun, G. C. Guo, C. T. Au and S. L. Suib, *Appl. Catal. B: Environ.*, 2014, 156–157, 447–455.

13. L. Xie, Z. Liu, J. Zhang and J. Ma, *J. Alloys Compd.*, 2010, 503, 159-162.

14. F. Duan, Y. Zheng and M. Q. Chen, *Mater. Lett.*, 2010, 65, 191-193.

15. J. Long, S. Wang, H. Chang, B. Zhao, B. Liu, Y. Zhou, W. Wei, X. Wang, L. Huang and W. Huang, *Small*, 2014, 10, 2791-2795.

16. L. W. Zhang, T. G. Xu, X. Zhao and Y.F. Zhu, *Appl. Catal. B: Environ.*, 2010, 98, 138-146.

17. Z. Dai, F. Qin, H. Zhao, F. Tian, Y. Liu and R. Chen, *Nanoscale*, 2015, 00, 1-5.

18. R.P. Rastogi, A.K. Singh, C.S. Shukla, J. Solid State Chem.,1982, 42, 136.

17. A. Martinez-de La Cruz, S.O. Alfaro, J. Mol. Catal. A: Chem. 2010, 320, 85.

18. L.M. Thang, L.H. Bac, I.V. Driessche, S. Hoste, W.J.M. Van Well, Catal. Today, 2008, 131, 566–571.

19. D. Saha, G. Madras and T.N. Guru Row, *Mater. Res. Bull.*, 2011, 46, 1252-1256.

20. M. Maczka, J. Hanuza, W. Paraguassu, A.G. Souza Filho, P.T. Freire and C.J. Mendes Filho, *Appl. Phys. Lett.*, 2008, 92, 112911-112914.

21. S. J. Liang, R. W. Liang, L. R. Wen, R. S. Yuan, L. Wu and X. X. Fu, *Appl. Catal., B*, 2012, 125, 103-110.

22. L. H. Chia, X. Tang and L. K. Weavers, *Environ. Sci.Technol.*, 2004, 38, 6875-6880.

23. A. Martinez-de La Cruz and S.O. Alfaro, *J. Mol. Catal. A: Chem.*, 2010, 320, 85-91.

24. S.R.G. Carrazan, C. Martin, V. Rives, R. Vidal, Spectrochim. Acta A, 1996, 52:1107-1118.

25. F. Trifiro H. Hoser and R. Scarle, J. Catal., 1972, 25:12-24.

26. W. D. Kovats and C.G Hill.Appl. Spectrosc., 1986 40:1215-1219.

27. N. Kim, R.N. Vannier and C.P. Grey, *Chem. Mater.*, 2005,17, 1952-1958.

28. W. H. Leng, Z. Zhang, J. Q. Zhang and C. N. Cao, *J. Phys. Chem. B*, 2005, 109, 15008-15023.